Dissipation, geometry, and the stability of the dense radial morphology

David G. Grier and Daniel Mueth
The James Franck Institute, The University of Chicago, 5640 S. Ellis Avenue, Chicago, Illinois 60637
(Received 28 June 1993)

The dense radial morphology appears in a number of systems undergoing branched growth. Neither ordered nor fractal, this pattern is characterized by a large number of branches radiating from a central seed and advancing behind a circular envelope. We propose a model for dense radial growth which self-consistently incorporates dissipation in the growth channels. A linear stability analysis of this model delimits conditions under which the dense radial morphology can develop. Predictions of this model are borne out by numerical simlations of evolving resistor bond networks.

PACS number(s): 68.70.+w, 47.54.+r, 61.43.Bn

I. DISSIPATION IN DIFFUSIVE PATTERN-FORMING SYSTEMS

Dissipation arises in most pattern-forming systems. Patterns developing in fluid flows dissipate energy through the fluids' viscosities. Electrochemical deposition is subject to Ohmic dissipation and to losses from convective motion of the electrolyte. Lightning bolts expend their energy in creating and heating a plasma whose expansion produces thunder. In these and other cases, dissipation alone does not govern the evolution of form. It can, however, qualitatively influence the outcome.

We shall confine our attention to patterns such as Fig. 1 in which fine branches radiate from a central seed and whose growth requires a current to flow along the branches. Such systems have been studied extensively over the past 30 years and produce both regular and lushly disordered patterns. Over some range of experimental parameters, many such systems produce well-developed stochastic fractals resembling diffusion-limited aggregation (DLA) [1,2]. The example in Fig. 1 is striking precisely because it is not fractal. Despite its random branching, it has a uniform areal density and is circumscribed by a smooth circular envelope. This shape has been dubbed the dense radial morphology [3,4] and its origin has been the subject of some dispute.

Previous analyses [5,6] of dissipation's role in forming dense morphologies have relied on two assumptions. Dissipation was treated as a contribution to the boundary condition at the interface between the advancing and retreating media. Currents within the advancing medium, furthermore, were assumed to flow strictly radially along the branches. Indeed, if this condition were relaxed and azimuthal currents allowed, the interfacial boundary condition would no longer be self-consistent.

The assumption that currents flow preferentially along branches seems appropriate to electrochemical deposition. In this system, growth proceeds through the accretion of ions onto an electrode. Ions flow to growth sites through an electrolytic solution and their charge is carried away as an electric current passing through the aggregate. Not only are metallic branches better conductors than electrolytic solutions, but also Fukunaka, Yamamoto, and Kondo have demonstrated that the solution between branches is depleted of charge carriers [7]. Viscous fluids injected into porous media similarly might have their flows constrained by fluid trapped in interstices [8,9]. Melrose and Hibbert [10], however, have shown that such anisotropy is not complete in electrochemical deposition. The appearance of closed loops in viscous flows through porous media indicate the limits of anisotropy for that system also [11,12]. Any effort to as-

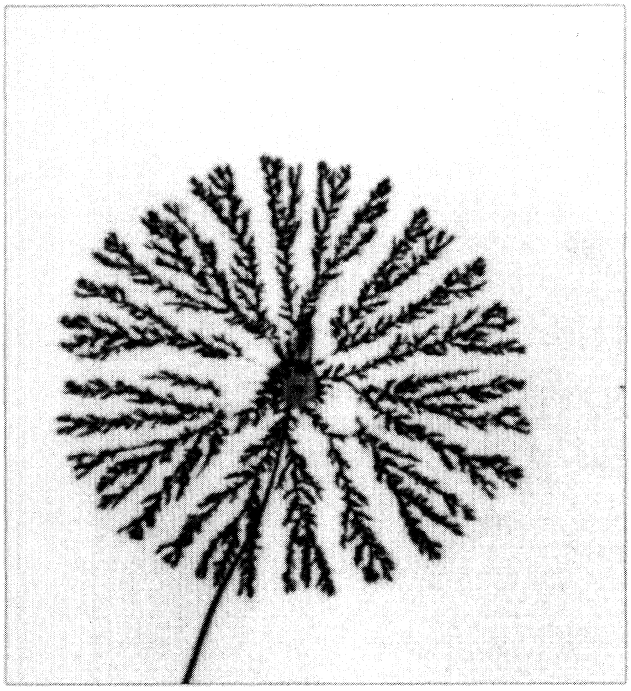

FIG. 1. Quasi-two-dimensional cadmium electrodeposit grown according to the method of Refs. [3,4]. The pattern is approximately 2 cm in diameter and 200 μm thick. It grew from a grounded cathode wire 0.1 mm in diameter. The outer ring anode, not visible in this picture, is 6.3 cm in diameter and was held at 20.26 V during the deposition. A film of 0.1M $CdSO_4$ aqueous solution provided the growth medium.

cribe the stability of the dense radial morphology to dissipation in the growth channels must treat the local structure and currents with some care.

In Sec. II, we introduce a simple yet realistic model for branched growth with dissipation. A linear stability analysis of this model predicts a nontrivial crossover from highly unstable, presumably branched interfaces to interfaces which are linearly stable at long wavelengths, as a function of growth conditions. These latter interfaces we identify with the dense radial morphology. This model also suggests that initially disordered aggregates can undergo a dynamic morphology transition into uniform dense radial aggregates if their conductivity is sufficiently anisotropic. Under a more restricted set of conditions, some stable aggregates can become unstable once again as they approach the bounds of their system. In Sec. III we test these ideas through numerical simulations of evolving resistor bond networks.

II. MODELING DISSIPATIVE GROWTH CHANNELS

A. Equations of motion

For simplicity, we will consider radial growth in two dimensions, although the approach can be generalized to three dimensions. Figure 2(a) depicts the radial variant of the model geometry. If we assume that the advancing medium has already formed a dense radial structure of radius r_0, then its envelope advances under the control of local currents, $\mathbf{j}_i$, with a normal velocity:

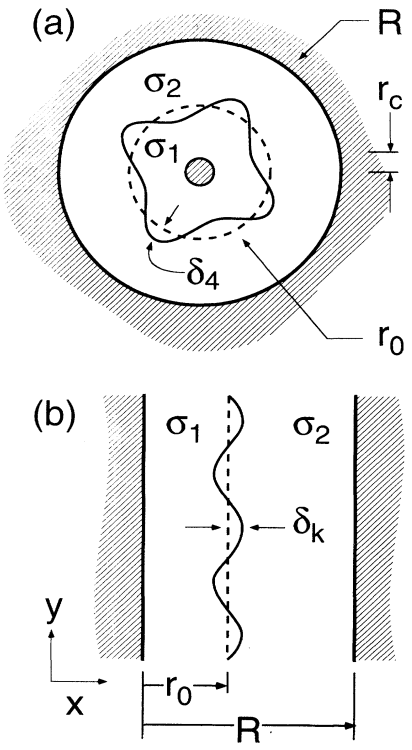

FIG. 2. Schematic diagram of the radial (a) and planar (b) growth geometries. The labeled quantities are described in the text.

$$v_0 = b\hat{\mathbf{n}}\cdot\mathbf{j}_i|_{r=r_0} . \tag{1}$$

The subscript i denotes either the advancing ($i=1$) or retreating ($i=2$) medium, and b is a system-dependent material parameter. Currents in turn arise from gradients of the underlying field through constitutive relations:

$$\mathbf{j}_i = \sigma_i \nabla u_i , \tag{2}$$

whose conductivities, σ_i, describe dissipation mechanisms. The sign convention in Eqs. (1) and (2) is determined by the particular system. Since this convention also determines signs in the boundary conditions, the results are unaffected.

We assume that the conductivity in the retreating medium, σ_2, is homogeneous and isotropic. To account for the inhomogeneity of the advancing medium, we treat its conductivity as a tensor. The simplest model reflecting a radially branched structure is

$$\sigma_1 = \begin{bmatrix} \sigma_r & 0 \\ 0 & \sigma_\theta \end{bmatrix} \tag{3}$$

in polar coordinates, where σ_r and σ_θ are constants. Equation (3) simply states that currents flow with different ease along and between the radially directed branches. The size, separation, and detailed geometry of the branches arise from a variety of system-dependent mechanisms [13,14]. Some of these effects also may affect pattern formation at long length scales, for example in electrochemical deposition where the interplay of drift, diffusion, and hydrodynamic flows are particularly complex. Since our aim is to elucidate the generic large-scale features of the dense radial morphology, we will take the small-scale local structure to be given and ignore other system-specific effects.

Conservation of the diffusion field in the quasistatic limit yields the equation of motion within the advancing medium

$$\frac{1}{r}\frac{\partial}{\partial r} r \frac{\partial u_1}{\partial r} + \frac{\gamma^2}{r^2}\frac{\partial^2 u_1}{\partial \theta^2} = 0 , \tag{4}$$

where $\gamma = \sqrt{\sigma_\theta/\sigma_r}$ measures the conductivity anisotropy in the advancing medium. The field in the displaced medium obeys Laplace's equation in the quasistatic limit:

$$\nabla^2 u_2 = 0 . \tag{5}$$

The combined fields satisfy the following boundary conditions:

$$u_1(r_c,\theta,t) = 0 , \tag{6a}$$

$$u_2(R,\theta,t) = 1 , \tag{6b}$$

$$u_1(r_s,\theta,t) = u_2(r_s,\theta,t) , \tag{6c}$$

$$j_1(r_s,\theta,t) = j_2(r_s,\theta,t) , \tag{6d}$$

where r_c is the radius of the central boundary, R is the radius of the enclosing boundary, and r_s is the radius of the interface at angle θ and time t. A term describing surface tension was not included in Eq. (6c) as it would have contributed only at short wavelengths, while we are

concerned with the long-wavelength stability of the morphology. Taking the quasistatic limit simplifies the calculations and permits direct comparison with the numerical simulations which we will present below. The corresponding assumption that the system has a long diffusion length is not required to stabilize the dense radial pattern. Rather, short diffusion lengths should tend to enhance the stability [5]. Screening within the displaced medium, which introduces another length scale into the problem, also has been shown to induce morphological transitions [15] but is not considered here.

B. Linear stability analysis

Without too much effort, we find that an initially circular interface with $r_s = r_0$ preserves its shape under Eqs. (4)–(6) and advances at the rate

$$v_0 = \frac{b\sigma_r}{r_0}\left[\ln\left[\frac{r_0}{r_c}\right] + \frac{\sigma_r}{\sigma_2}\ln\left[\frac{R}{r_0}\right]\right]^{-1} . \tag{7}$$

To determine the stability of this solution against arbitrary perturbations, we follow Mullins and Sekerka [16] in noting that any such perturbation can be decomposed into Fourier components, and calculate the growth rate of each component independently. These growth rates emerge as solutions to Eqs. (4)–(6) for the perturbed circular boundary $r_s = r_0 + \delta_m \exp(im\theta)$, which we calculate to linear order in the infinitesimal amplitude, δ_m. The index m refers to the Fourier component with m lobes. If the normalized growth rate of the mth mode, $\alpha_m = (\dot{\delta}_m/\delta_m) r_0/v_0$, is positive, then an infinitesimal m-fold perturbation will grow sufficiently rapidly to become evident within the finite duration of an experiment. If α_m is negative, then the interface is stable against m-fold perturbations.

Solving Eqs. (4)–(6) for a perturbed circular interface, we find

$$\alpha_m = -1 + m f_m(r_0) , \tag{8a}$$

where

$$f_m(r_0) = \frac{\gamma(\xi - 1)}{\tanh[m\gamma \ln(r_0/r_c)] + \gamma\xi \tanh[m \ln(R/r_0)]} . \tag{8b}$$

In Eq. (8b) we have defined the conductivity contrast $\xi = \sigma_r/\sigma_2$ which is the reciprocal of the control parameters defined in Refs. [5,6].

Typical representations of α_m appear in Fig. 3. The first insight we draw from Eq. (8) and Fig. 3 is that the moving interface is linearly stable at all wavelengths when there is no conductivity contrast: $\alpha_m|_{\xi=1} = -1$. Uniform stability of all models is not surprising under these conditions. With no conductivity contrast, the interface between the two media is simply a notational convenience. Thus the tip of a perturbation advances at the same rate as a circular interface of radius $r_0 + \delta_m$ while its trough advances at the rate appropriate to the radius $r_0 - \delta_m$. Since the interfacial velocity decreases with radius [Eq. (7)] the troughs overtake the peaks and the perturbations shrink. Thus the fundamental stability of the dense radial pattern arises simply from the geometry of the system.

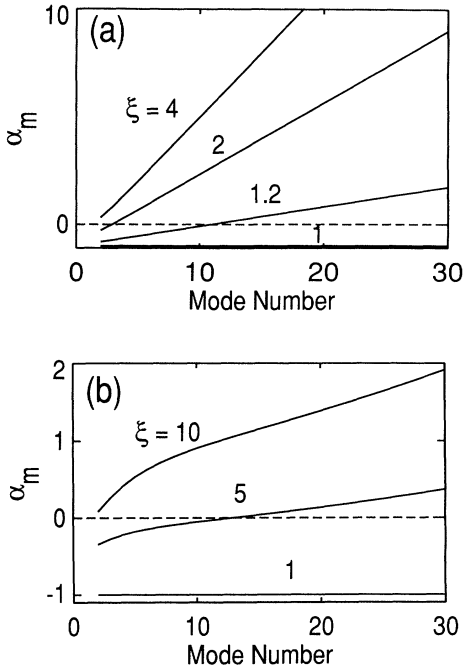

FIG. 3. Normalized growth rate of distortion modes predicted in Eq. (8) for a system with $x = r_0/R = 0.5$ and $r_c/R = 0.01$. Those modes with $\alpha_m < 0$ are stable, while those with $\alpha_m > 0$ are unstable. Curves are parametrized by conductivity contrast, ξ. (a) Isotropic limit: $\gamma = 1$. (b) Anisotropic limit: $\gamma = 0.01$.

When $\sigma_r < \sigma_2$, all modes are linearly stable and the interface advances as a circle without branches. This corresponds to forcing a viscous fluid to displace an inviscid one. The converse case, where $\sigma_r > \sigma_2$, leads to a richer phenomenology. If the conductivity contrast is large, then all modes are linearly unstable and the interface devolves into disorder. Smaller contrasts, however, leave a range of stable modes with mode numbers smaller than a critical value, m_c. This is the regime in which the dense radial morphology appears. Stability of long-wavelength modes accounts for the overall circular shapes of the dense radial aggregates. Instability at high mode number permits aggregates to have a large number of finely divided branches. The underlying assumptions in the model about the geometry of the aggregates are self-consistent.

Patterns evolving according to Eq. (8) can pass through two morphological transitions as they grow. To show this, we examine the marginally stable mode number, m_c, for which $\alpha_m(r_0) = 0$. Values of m_c are computed as real roots of the transcendental equation

$$\xi = \frac{\gamma m + \tanh\left[m\gamma \ln\left[\frac{r_0}{r_c}\right]\right]}{\gamma m - \gamma \tanh\left[m \ln\left[\frac{R}{r_0}\right]\right]} . \tag{9}$$

Plots of m_c as a function of $x = r_0/R$ appear in Fig. 4 for a variety of growth conditions.

In the limit of strong anisotropy [Fig. 4(b)], initially unstable long-wavelength modes rapidly stabilize when the aggregate reaches the nearly vertical marginal stability curve. Under these conditions, instabilities have no opportunity to grow and the aggregate is dense and radially symmetric essentially from its inception. Increasing the conductivity contrast moves the marginal stability line out to large radii so that early stage instabilities have time to grow. Early growth perturbations disappear once an aggregate passes the marginal stability line provided that nonlinearities have not come to dominate the dynamics.

Qualitative evidence for such a crossover is provided by experiments in electrochemical deposition in which initially disordered aggregates develop into dense radial structures as they grow. The disorder in early stage growth is still evident in the lacunae near the center of the aggregates such as the example in Fig. 1. Presumably because disorder engendered in early growth can produce strongly nonlinear dynamics, not all electrodeposits grown in this regime are dense radial.

Referring once again to Fig. 4(b), we see that sufficiently large conductivity contrasts render all modes linearly unstable for aggregates of all sizes. Between the limits of strong and weak conductivity contrast, however, there are some conditions for which the marginal stability curve is nonmonotonic. Under such conditions, an initially disordered aggregate could cross over first into the dense radial pattern and subsequently devolve into disorder as it grows. That such a two-stage dynamic morphology transition has not been reported is not surprising as it should occur over only a very limited range of experimentally accessible parameters. Furthermore, few experimental studies have focused on the evolution of long-wavelength modes in the parameter regime of interest.

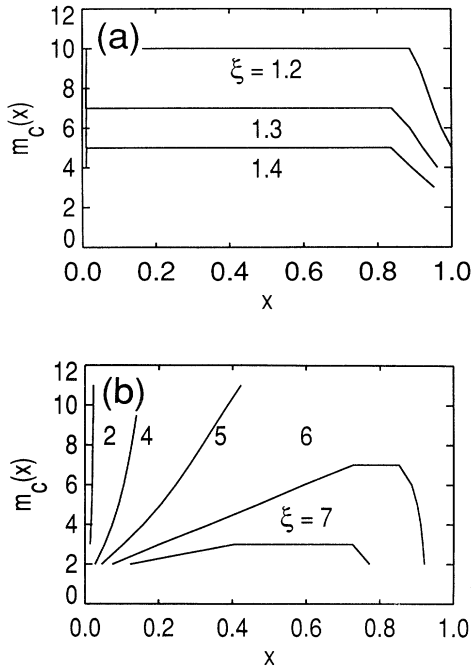

FIG. 4. Marginally stable mode number as a function of aggregate size. For a given size, perturbations with mode numbers above a given curve are unstable, while all those below are stable. Curves are parametrized by conductivity contrast, ξ. (a) Isotropic limit: $\gamma = 1$. (b) Anisotropic limit: $\gamma = 0.01$. The crossover from instability to stability at $\xi = 5$ is predicted to occur at such large radii that we expect nonlinearities to overwhelm the linear stabilizing mechanism.

Weak anisotropy, $\gamma \approx 1$, removes virtually all of the size dependence from the stability of modes, as can be seen in Fig. 4(a). A dense aggregate growing under these conditions will be stable at long wavelengths and should have a uniform areal density. Indeed, dense radial flows in porous media, which have a relatively small anisotropy, do not leave large gaps near their centers [17]. The isotropic low-conductivity-contrast regime has been studied by real-space renormalization-group methods [18], numerically [19], and experimentally [20]. Our results are consistent with crossovers evident in these studies although none investigated in detail the region of parameter space which we have identified with morphological crossovers. Also, these studies did not investigate the mode number dependence of interfacial stability.

As a counterpoint to these results, we present analogous calculations of a linear interface advancing in a planar geometry [Fig. 2(b)]. In this case, the interface advances at a rate

$$v_0 = \frac{\sigma_x b}{r_0 + \frac{\sigma_x}{\sigma_2}(R - r_0)} \tag{10}$$

and the spectrum of instabilities is found to be

$$\alpha_k = \frac{kr_0\gamma\left[\frac{\sigma_x}{\sigma_2} - 1\right]}{\tanh(\gamma k r_0) + \gamma\frac{\sigma_x}{\sigma_2}\tanh[k(R - r_0)]}, \tag{11}$$

where k is the wave number of the perturbation, σ_x is the conductivity in the growth direction, and all other variables are defined as they were in the radial case. When there is no mobility contrast, the interface is only marginally stable at all wavelengths. If $\sigma_x > \sigma_2$, then the linear front is linearly unstable against perturbations at all wavelengths regardless of the conductivity anisotropy. This result differs qualitatively from the radial case and emphasizes that the dense radial morphology arises not only from dissipation in the growth channels, but also from the geometry of the system as a whole.

Simulations of growth without anisotropy in the planar geometry [17] show no evidence of long-wavelength stability. Experiments in quasi-two-dimensional electrochemical deposition between parallel line electrodes sometimes evince linear growth fronts. It seems reasonable to ascribe this observed stability to factors such as short diffusion lengths ahead of the growth front which have been shown to enhance stability at long wavelengths [5].

III. NUMERICAL SIMULATIONS

A. Evolving resistor-bond-network model

We have tested these ideas through numerical simulations of resistor bond networks similar to those previously used to simulate dielectric breakdown [21] and viscous flows [12,17,22]. Resistors are arranged on a triangular lattice with boundary conditions imposed at the central node and along a hexagonal border to model the outer boundary conditions of Eq. (6b). The hexagonal outer boundary is a circle in lattice metric and has a diameter of 200 bonds in our simulations. The growing aggregate and displaced medium are represented by bonds of conductance C_a and C_m, respectively. Conductivity anisotropy is introduced by setting the conductance between neighboring aggregate nodes which are not contiguous on the same branch to C_b. This arrangement is depicted in Fig. 5. Although $\gamma=\sqrt{C_b/C_a}$ corresponds only roughly to the conductivity anisotropy defined above, the insensitivity of m_c to variations in γ for small γ suggests that comparisons between the model and simulations in this regime should be reasonable. Comparisons in the isotropic limit, $\gamma=1$, similarly should be reasonable.

Before each growth step, local potentials throughout the network are iteratively relaxed until Kirchoff's law is satisfied to better than 5 parts in 10^4 at each node. Thus the simulations represent the quasistatic limit of the growth model. At each step, one of the surface bonds is randomly selected to grow with a probability proportional to the current through that bond. This bond and its node are then added to the aggregate, the neighboring bonds are updated to reflect the new connectivity, and the process is repeated. Typical simulations appear in Fig. 6. When the invading and displaced media have identical conductivities, dense Eden-like aggregates such as the example in Fig. 6(a) result. The opposite extreme, which corresponds to an inviscid fluid displacing a viscous fluid, leads to open DLA-like structures as in Fig. 6(b). The structures emerging in these extreme limits of conductivity contrast are not affected qualitatively by variations in the conductivity contrast. In the first case, currents naturally flow radially inward, bypassing the interbranch bonds, and in the latter the branches are so separated that very few of interbranch bonds are ever created. Where conductivity anisotropy plays a role is in the transition from Eden-like to DLA-like structures.

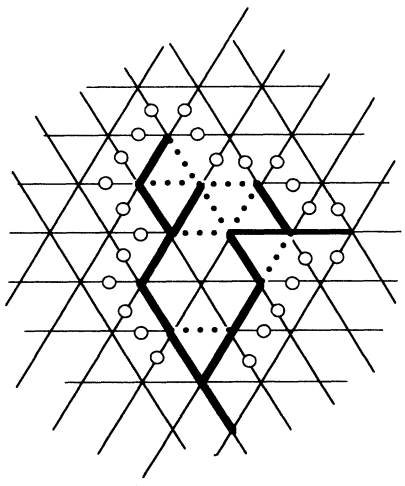

FIG. 5. Assignment of resistor values in a small section of a network simulation. Heavy lines represent aggregate bond with conductance C_a. Light lines represent bonds between nodes of the surrounding medium, C_m. Dotted lines represent bonds between aggregate sites on different branches, C_b. Circles denote the "surface" of the aggregate as defined in the text. An example of such a surface appears in Fig. 8.

The triangular lattice was selected to minimize the effects of lattice anisotropy both on the calculation of the potential and also on the morphology of the aggregate [23]. These effects could be further reduced by performing off-lattice simulations, but at a considerably higher computational cost. Numerical techniques such as simultaneous overrelaxation and Chebychev acceleration do not work well for these simulations because the conductance of the network changes at every step, requiring corresponding changes in the acceleration parameters. We do, however, decompose the triangular lattice into four sublattices such that the potential at each node in any one sublattice depends only upon the potentials in the other three. Each relaxation step then consists of calculating corrections for each sublattice in sequence.

The growth algorithm imposes two additional conditions: no branches are allowed to form between existing branches, and no bonds or aggregate sites are allowed to disappear. The inability to form bridges or disconnected islands renders these simulations less than ideal representations of viscous fingering in porous media [12] but is entirely appropriate to electrochemical deposition and dielectric breakdown. These issues arise in the simulations, as they do in experiments, because field gradients developing around circuitous branches can favor a transfer of material to shorter neighboring branches. This is handled in our simulations by not counting such negative surface currents when determining a bond's growth probability.

An aggregate's interface is defined as the locus of centers of bonds connecting the aggregate to the outside lattice. These centers appear as circles in Fig. 5. This definition ensures that the interface, described in polar coordinates as $r_s(\theta)$, does not cross itself although it may be a multiple-valued function of θ. Because aggregates growing in the dense radial regime should have few overhangs, such multiple-valued regions negligibly affect Fourier descriptors of $r_s(\theta)$ at long wavelengths. Single-valued representations such as the curvature parametrized by arc length of the interface overemphasize short-wavelength features and so were not used in this analysis.

We find that fast-Fourier-transform (FFT) algorithms are not appropriate for measuring amplitudes of long-wavelength modes: numerical errors amassed in treating individual branches swamp the relatively weak features of the overall envelope. Instead, we calculate each mode's amplitude independently:

$$\delta_m e^{i\phi_m}=\frac{2}{N}\sum_{i=1}^{N}(r_i-r_0)e^{im\theta_i}\,, \tag{12}$$

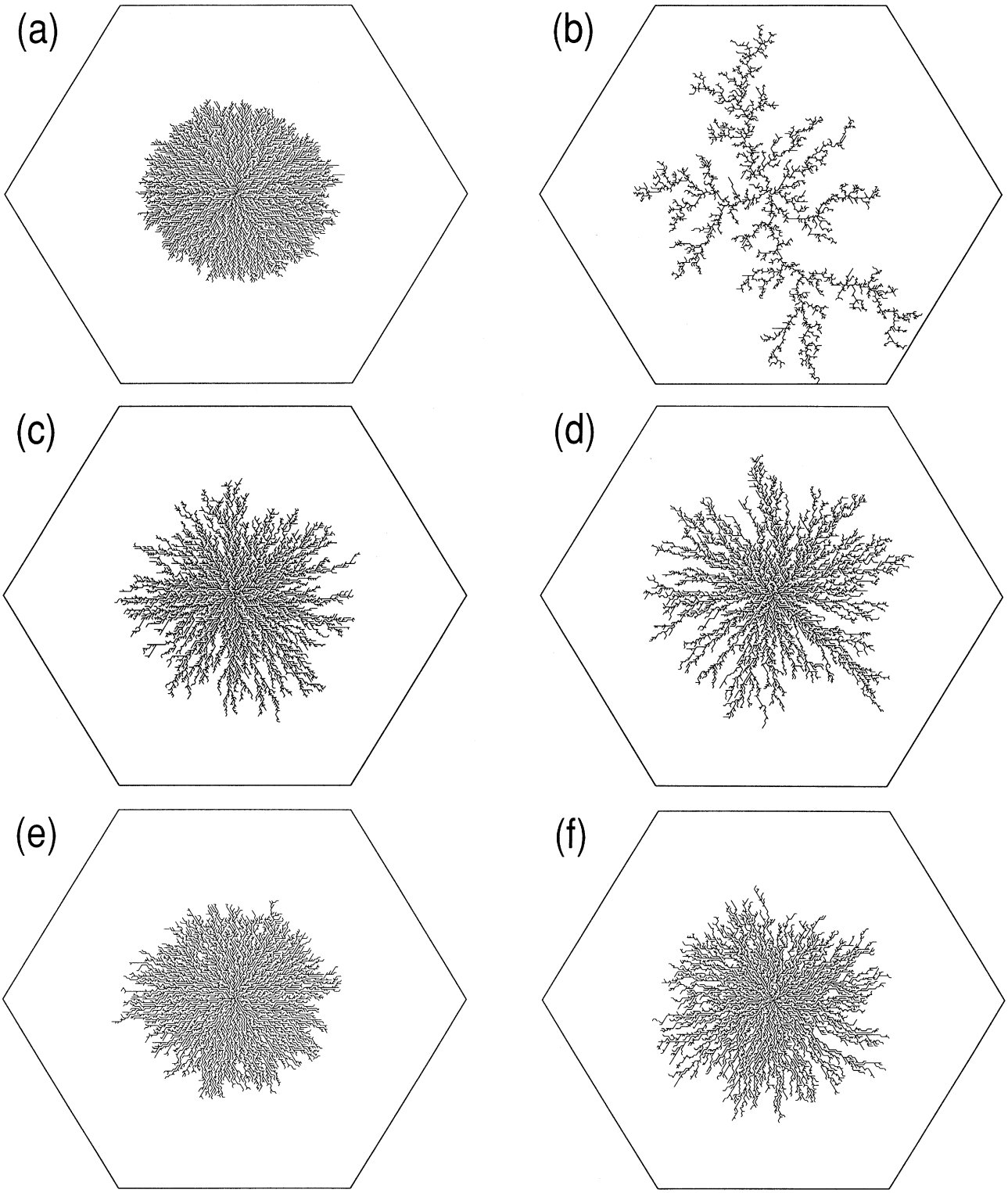

FIG. 6. Typical simulations of evolving resistor bond networks. The location of the outer boundary is drawn with heavy lines and has a lattice metric radius of 100 bonds. Examples (a) and (b) demonstrate the behavior of the growth algorithm in the Eden ($\xi=1$) and DLA ($\xi=10^6$) limits, respectively. Although both aggregates were grown with $\gamma=1$, the same qualitative results appear for all values of γ. Examples (c)–(f) demonstrate the role of current confinement in stabilizing the aggregate envelope. (c) and (d) are grown in the isotropic limit $\gamma=1$, while (e) and (f) are grown in the anisotropic limit $\gamma=10^{-2}$: (c) Unstable: $\xi=4$. (d) Unstable: $\xi=7$. (e) Dense radial: $\xi=4$. (f) Unstable: $\xi=7$. All aggregates except (b) are shown at the stage where they contain 6000 bonds. Example (b) contains 3461 bonds.

where r_i and θ_i are the polar coordinates of the ith interfacial point measured with respect to the center. The average is taken over N interfacial points, and the radius of the undistorted interface is estimated [24] as

$$r_0^2 = \left[\frac{1}{2\pi} \sum_{i=2}^{N} (y_i x_{i-1} - x_i y_{i-1}) \right] .$$

Here x_i and y_i are the Cartesian coordinates of the interface locations. Unlike the FFT approach, Eq. (12) is readily amenable to irregularly gridded data and returns its amplitude in units of the bond length.

B. Isotropic limit

The aggregates in Figs. 6(a)–6(d) grew with interbranch conductance equal to the conductance of the branches themselves: $C_b = C_a$. The example in Fig. 6(a) corresponds to the case in which there is no conductivity contrast. This perfectly stable aggregate nonetheless has some surface roughness due to stochastic noise in the growth process. Typical distortion amplitudes at low mode numbers fall around half a bond length as measured with Eq. (12). As the conductance of the aggregate bonds is increased, from $C_a = 1$ in Fig. 6(a) to $C_a = 10^6$ in Fig. 6(b), the interface becomes increasingly disordered. The limit of large conductivity contrast corresponds to diffusion-limited aggregation, and the pattern in Fig. 6(b) displays the open ramified structure typical of DLA. A detailed analysis of the scaling behavior of such aggregates is not warranted because of their small size. The marginal stability curves in Fig. 4(a) indicate that for conductivity contrasts as small as $\xi = 1.5$, the interfaces of aggregates should already be unstable. Indeed, those aggregates in Figs. 6(c) with $\xi = 4$ and 6(d) with $\xi = 7$ already show a large and increasing degree of openness and disorder.

Figure 7(a) shows $\langle \delta_m \rangle$ as a function of filling fraction, $x = r_0/R$, for aggregates such as those in Figs. 6(a)–6(d), grown in the limit of small conductivity anisotropy. Here the angular brackets indicate averages over modes 4–10 and over one or two instances of aggregates grown independently under identical conditions. These mode numbers are selected as being representative of the long-wavelength structure of the various interfaces (Fig. 8). As predicted by the linear growth model, those aggregates grown with conductance contrasts greater than about 1.5 show rapidly diverging surface distortions at long wavelengths. Quite a different story emerges from growth in the strongly anisotropic limit.

C. Anisotropic limit

Growth conditions for the aggregates in Figs. 6(e) and 6(f) correspond to those for Figs. 6(c) and 6(d) except for their strong conductivity anisotropy: $\gamma = 10^{-2}$. According to the analysis of Sec. II, an aggregate such as that in Fig. 6(e) with $\xi = 4$ should become stable at long wavelengths. After some scrutiny, this aggregate looks qualitatively rounder and smoother than its isotropic counterpart in Fig. 6(c). By increasing the conductivity contrast to $\xi = 7$, we cross over to the disordered regime, as the aggregate in Fig. 6(f) shows.

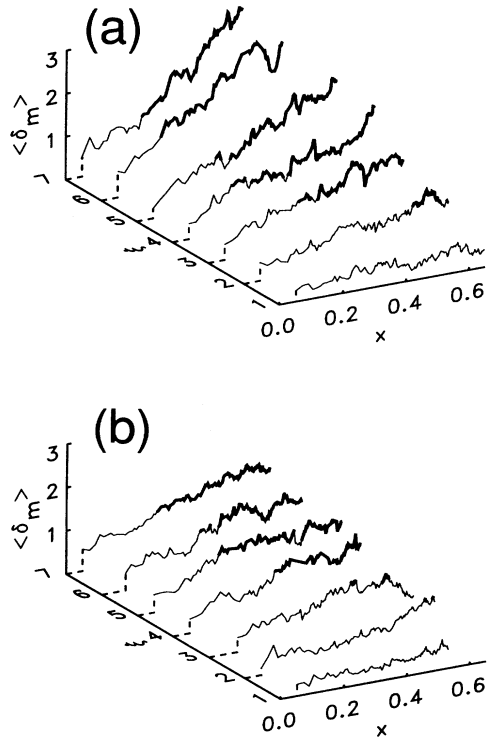

FIG. 7. Amplitudes of long-wavelength modes, $\langle \delta_m \rangle$, measured with Eq. (12) and averaged over mode numbers 4–10 and over one or two realizations of each set of growth conditions. Data are plotted as a function of aggregate size $x = r_0/R$ and conductivity contrast, ξ. (a) Isotropic limit: $\gamma = \sqrt{C_b/C_m} = 1$. (b) Anisotropic limit: $\gamma = 10^{-2}$. Those measurements with distortion amplitudes $\langle \delta_m \rangle$ larger than a single bond length are considered unstable and are plotted with a heavy line.

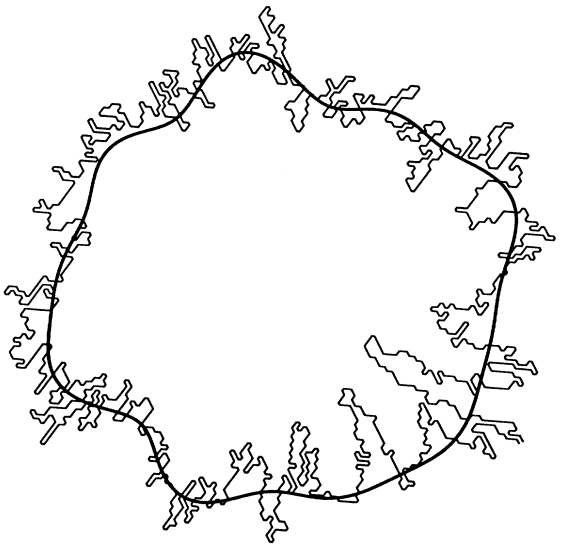

FIG. 8. Interface of the aggregate in Fig. 6(f) overlaid with an interface reconstructed from Fourier modes 4–10.

We identify aggregates such as that in Fig. 6(e) with the dense radial morphology. This pattern appears considerably less stable at long wavelengths than the experimental realization in Fig. 1 because the simulations produce comparatively small aggregates. In both experiment and simulation, interfacial roughness arises from stochastic noise. If the amplitude of this noise-driven roughness remains constant as the aggregate grows, then eventually the interfacial roughness will become negligible on the scale of the entire pattern.

The identification of aggregates such as that in Fig. 6(e) with the dense radial morphology rests on the measurements of low-mode-number distortions plotted in Fig. 7(b). Again taking $\langle \delta_m \rangle = 1$ to be the distortion amplitude at which an interface is considered unstable, we see that runs with ξ smaller than 4 remain stable throughout their growth. Not only are these distortion amplitudes small, but also they do not grow. The absolute growth rate of perturbations remains vanishingly small for runs with ξ smaller than 5 or 6. All of these aggregates are dense radial. As ξ is increased, aggregates become increasingly unstable at smaller sizes. This crossover from stable to unstable growth as a function of growth conditions agrees with the crossover predicted in the preceding analysis as depicted in Fig. 4(b).

IV. DISCUSSION

Quantitative analysis of the evolution of interfacial distortions in our simulations supports our contention that dissipation, geometry, and current confinement all contribute to the stability of the dense radial morphology. In particular, the crossover predicted by our growth model to occur for anisotropic aggregates near $\xi = 5$ is in very good agreement with the measured evolution of long-wavelength distortions in our simulations. The interfacial stability observed for those simulations we identify with the dense radial morphology leads us to project that larger simulations would more visibly resemble the dense radial patterns realized experimentally.

We have seen no unequivocal evidence of the dynamic crossover from early stage disorder to later stage dense radial structure in any of our simulations. Nor have our simulations revealed the second dynamical crossover to late stage disorder. We believe that the apparent absence of these transitions also is due to the very limited scale and coarse graining of our simulations and look forward to experimental studies which should provide superior tests of these predictions.

ACKNOWLEDGMENTS

We gratefully acknowledge fruitful discussions with T. Witten and L. Sander. Oscar Pla was instrumental in arriving at a correct statement of Eq. (8). This work was supported in part by the Materials Research Laboratory of the University of Chicago and in part by the Petroleum Research Fund of the American Chemical Society through Grant No. 26872-G.

[1] T. A. Witten, Jr. and L. M. Sander, Phys. Rev. Lett. **47**, 1400 (1981).
[2] T. A. Witten and L. M. Sander, Phys. Rev. B **27**, 5686 (1983).
[3] Y. Sawada, A. Dougherty, and J. P. Gollub, Phys. Rev. Lett. **56**, 1260 (1986).
[4] D. Grier, E. Ben-Jacob, R. Clarke, and L. M. Sander, Phys. Rev. Lett. **56**, 1264 (1986).
[5] D. G. Grier, D. A. Kessler, and L. M. Sander, Phys. Rev. Lett. **59**, 2315 (1987).
[6] D. B. Hibbert and J. R. Melrose, Proc. R. Soc. London, Ser. A **423**, 149 (1989).
[7] Y. Fukunaka, T. Yamamoto, and Y. Kondo, J. Electrochem. Soc. **136**, 3278 (1989).
[8] J. P. Stokes, D. A. Weitz, J. P. Gollub, A. Dougherty, M. O. Robbins, P. M. Chaikin, and H. M. Lindsay, Phys. Rev. Lett. **57**, 1718 (1986).
[9] Y. C. Yortsos, J. Phys. Condens. Matter **2**, SA443 (1990).
[10] J. R. Melrose and D. B. Hibbert, Phys. Rev. A **40**, 1727 (1989).
[11] R. Lenormand, Physica A **140**, 114 (1986).
[12] J. D. Sherwood, J. Phys. A **19**, L195 (1986).
[13] V. Fleury, J.-N. Chazalviel, and M. Rosso, Phys. Rev. Lett. **68**, 2492 (1992).
[14] V. Fleury, M. Rosso, J.-N. Chazalviel, and B. Sapoval, Phys. Rev. A **44**, 6693 (1991).
[15] E. Louis, F. Guinea, O. Pla, and L. M. Sander, Phys. Rev. Lett. **68**, 209 (1992).
[16] W. W. Mullins and R. F. Sekerka, J. Appl. Phys. **34**, 323 (1963).
[17] J. D. Sherwood and J. Nittmann, J. Phys. (Paris) **47**, 15 (1986).
[18] T. Nagatani and H. E. Stanley, Phys. Rev. A **41**, 3263 (1990).
[19] M. J. King and H. Scher, Phys. Rev. A **41**, 874 (1990).
[20] V. Frette, K. J. Måløy, F. Boger, J. Feder, and T. Jøssang, Phys. Scr. **T38**, 95 (1991).
[21] L. Niemeyer, L. Pietronero, and H. J. Wisemann, Phys. Rev. Lett. **52**, 1033 (1984).
[22] P. R. King, J. Phys. A **20**, L529 (1987).
[23] T. A. Witten, R. Ball, and M. Nauenberg, Phys. Rev. A **29**, 2017 (1984).
[24] M. Seul, M. J. Sammon, and L. R. Monar, Rev. Sci. Instrum. **62**, 784 (1991).

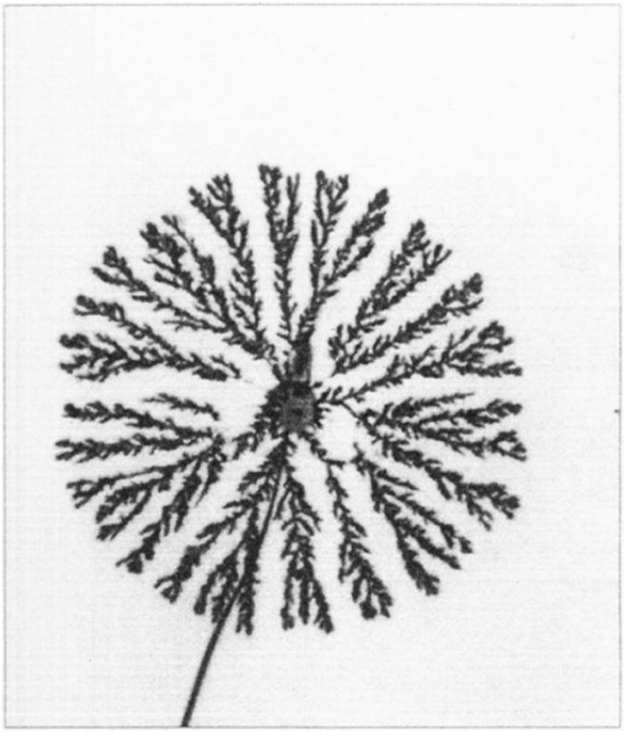

FIG. 1. Quasi-two-dimensional cadmium electrodeposit grown according to the method of Refs. [3,4]. The pattern is approximately 2 cm in diameter and 200 μm thick. It grew from a grounded cathode wire 0.1 mm in diameter. The outer ring anode, not visible in this picture, is 6.3 cm in diameter and was held at 20.26 V during the deposition. A film of 0.1M $CdSO_4$ aqueous solution provided the growth medium.